Electrochemical performance of spinel LiMn$_2$O$_4$ cathode materials made by flame-assisted spray technology

Xiaofeng Zhang [a], Honghe Zheng [b], Vincent Battaglia [b], Richard L. Axelbaum [a],*

[a] Department of Energy, Environmental and Chemical Engineering, Center for Materials Innovation, Washington University, One Brookings Drive, St. Louis, MO 63130, USA
[b] Advanced Energy Technology Department, Lawrence Berkeley National Laboratory, Berkeley, CA 94720, USA

ARTICLE INFO

ABSTRACT

Spinel lithium manganese oxide LiMn$_2$O$_4$ powders were synthesized by a flame-assisted spray technology (FAST) with a precursor solution consisting of stoichiometric amounts of LiNO$_3$ and Mn(NO$_3$)$_2$·4H$_2$O dissolved in methanol. The as-synthesized LiMn$_2$O$_4$ particles were non-agglomerated, and nanocrystalline. A small amount of Mn$_3$O$_4$ was detected in the as-synthesized powder due to the decomposition of spinel LiMn$_2$O$_4$ at the high flame temperature. The impurity phase was removed with a post-annealing heat-treatment wherein the grain size of the annealed powder was 33 nm. The charge/discharge curves of both powders matched the characteristic plateaus of spinel LiMn$_2$O$_4$ at 3 V and 4 V *vs.* Li. However, the annealed powder showed a higher initial discharge capacity of 115 mAh g^{-1} at 4 V. The test cell with annealed powder showed good rate capability between a voltage of 3.0 and 4.3 V and a first cycle coulombic efficiency of 96%. The low coulombic efficiency from capacity fading may be due to oxygen defects in the annealed powder. The results suggest that FAST holds potential for rapid production of uniform cathode materials with low-cost nitrate precursors and minimal energy input.

© 2010 Elsevier B.V. All rights reserved.

1. Introduction

Spinel lithium manganese oxide LiMn$_2$O$_4$ and its derivatives have gained attention as an alternative to lithium cobalt oxide (LiCoO$_2$), which is currently being used commercially as a cathode material for lithium-ion secondary batteries. Spinel LiMn$_2$O$_4$ has many desirable advantages, including high rate performance due to its 3D framework, high energy density, low cost, low toxicity, and simplicity of preparation [1]. The conventional approach to synthesis of LiMn$_2$O$_4$ spinel is the solid-state reaction of a mixture of lithium and manganese precursors at high temperature [2]. Sometimes mechanical grinding (*e.g.,* ball milling) is needed to reduce particle size [3]. Other approaches to synthesis have been developed, including the Xerogel method [4], Pechini process [5], sol–gel method [6], sputtering [7], and coprecipitation [8]. These methods have been shown to produce powders that have narrow size distribution, and uniform composition and morphology, yielding good electrochemical performance. Nonetheless, none of these processes are continuous, and long reaction times are required.

In the past decade, spray pyrolysis, which is a continuous process, has been studied to synthesize fine LiMn$_2$O$_4$ powder and its derivatives, yielding materials with good electrochemical perfor-

mance [9–14]. Spray pyrolysis is an aerosol process that can involve gas-, liquid-, and solid-phase reactions. The as-synthesized particles are in the nano- to micron-size range and can have a variety of morphologies. Common spray pyrolysis processes include ultrasonic spray pyrolysis [11,15], electrospray pyrolysis [9], and spray drying [12]. In the spray pyrolysis process the precursor solution is aerosolized to form fine precursor droplets. The aerosolized precursor is then introduced into a tubular furnace reactor in which the solvent evaporates, and then the precursors precipitate and decompose forming the desired product [15]. Under certain conditions, shell-structured LiMn$_2$O$_4$ particles are present in the products and this lowers the packing density of the material [15,16]. Spray pyrolysis requires external heating to maintain reactor temperature and this non-uniform heating can lead to non-uniformities in product, making it difficult to scale up [17,18].

Flame synthesis is a widely used technique to synthesize a number of functional powders over a range of sizes from nano- to micrometers, *e.g.,* carbon nanotubes and carbon black [19–21], metal oxide particles (TiO$_2$, SiO$_2$, Y$_2$O$_3$:Eu) [22–24], and non-oxide ceramics (Ti, TiB$_2$, Ta, and AlN) [25–28]. Among them, carbon black is the most successful example with daily production of about 100 tons [21]. In flame synthesis, the exothermic reaction between fuel and oxidizer generates heat to create a high temperature environment. Thus, it does not require external heating, and the heating is volumetric in flames. By changing the flame temperature and precursor solution composition, crystal structure and particle sizes
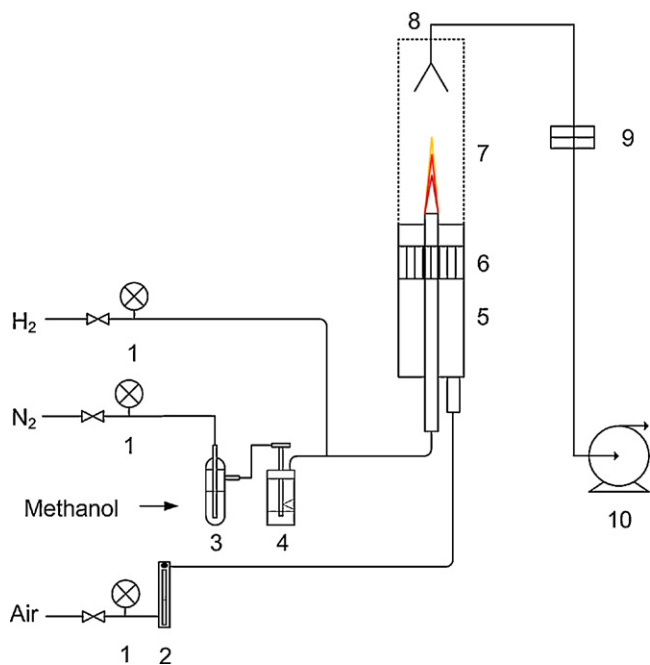
Fig. 1. Schematic diagram of the FAST setup: (1) pressure gauge, (2) flow meter, (3) methanol bubbler, (4) single-jet atomizer, (5) coflow burner, (6) honeycomb, (7) quartz chamber, (8) collection funnel, (9) filter, (10) vacuum pump.

can be varied. Hence, flame synthesis has the potential to produce cathode materials for lithium-ion batteries at a large scale and low cost.

Jang et al. have synthesized $LiCoO_2$ nanoparticles *via* flame spray pyrolysis (FSP) using H_2 as the fuel [29]. However, the electro-chemical properties of the as-synthesized $LiCoO_2$ nanoparticles were not evaluated in that work. Recently, Pratsinis et al. devel-oped an alternative FSP process to produce spinel-$LiMn_2O_4$ cathode materials using liquid-phase fuels [30,31]. In this process, metallic-organic compounds were dissolved in an organic solvent to serve as precursors. The as-produced spinel-$LiMn_2O_4$ showed a good rate capability at 4 V [32]. Nonetheless, the commercial viability of the FSP process is highly dependent on the price, availability, and compatibility of the metallic-organic precursor compounds and solvents. In the present work, a flame-assisted spray technol-ogy (FAST) is developed to produce spinel $LiMn_2O_4$ powders using low-cost metal-nitrate precursors.

2. Experimental

2.1. Powder synthesis

Fig. 1 shows a schematic diagram of the FAST experimen-tal setup, using a hydrogen laminar-diffusion-flame to synthesize spinel $LiMn_2O_4$. The inner jet of the co-flow burner has a 10.9 mm inner diameter and is made of 316-stainless steel. A honeycomb structure surrounding the jet ensures a uniform laminar flow of air, and an open-ended cylindrical quartz chamber is used to shield the flame from the ambient environment. The precursor was prepared by dissolving stoichiometric quantities (1:2 molar ratio) of $LiNO_3$ and $Mn(NO_3)_2 \cdot 4H_2O$ in methanol. The concentrations of $LiNO_3$ and $Mn(NO_3)_2$ were 0.5 mol L^{-1} and 1.0 mol L^{-1}, respectively. The pre-cursor aerosol was generated with a one-jet Collison atomizer (BGI Inc.) in methanol-saturated N_2 atomizing gas, where the inlet pres-sure was maintained at 193 kPa. The atomizing gas was saturated with methanol vapor prior to entering the atomizer to prevent evaporation of solvent methanol, thus maintaining a constant pre-cursor concentration. The flow rates of H_2 and the atomizing gas N_2

were kept at 0.5 L min^{-1} and 2.5 L min^{-1}, respectively. The flame temperature was measured with a Pt/Rh thermocouple inserted into the flame. The data was recorded with an Omega wireless thermocouple connector. To improve the grain sizes and remove impurity phases, the flame-synthesized powder was annealed at 700 °C for 2 h. The heating rate was 10 °C min^{-1} from room tem-perature to 700 °C, and the cooling rate was 3.3 °C min^{-1}.

2.2. Analysis and characterization

The decomposition temperature of the precursors was evaluated *via* thermogravimetric analysis (TGA). The $LiNO_3$/$Mn(NO_3)_2 \cdot 4H_2O$/methanol precursor solution was isother-mally heated at 50 °C for 1 h to completely evaporate the methanol solvent; then the temperature was ramped to 800 °C at 10 °C min^{-1}. Particle size distribution of the as-synthesized aerosol was mea-sured with a scanning mobility particle sizer (SMPS) by extracting the aerosol with a glass probe at 40 cm from the burner exit. The as-synthesized powder was collected with a Nuclepore Track-etch polycarbonate membrane filter (pore size 0.2 μm) downstream of the flame. An X-ray diffractometer (Rigaku D-MAX/A) was used to acquire the crystallographic parameters and crystal structure of the powder. The scanning range was from 10° to 70° with a step size of 0.04°. The grain size of the annealed powder was calculated using the Scherrer equation from the full-width at half maximum (*fwhm*) of the (400) plane of the XRD pattern. The elemental composition of the as-synthesized powder was analyzed with an inductively-coupled-plasma mass spectrometer (ICP-MS, Agilent 7500ce). The particle morphology was examined with a scanning electron microscope (SEM, JEOL7001LVF) and transmission electron microscope (TEM, JEOL2100F).

2.3. Electrochemical performance measurement

2032 coin-type test batteries were assembled and tested with flame-synthesized powder as the cathode active materials. To pre-pare the cathode, a mixture of the $LiMn_2O_4$ powder, polyvinylidene fluoride (PVdF) binder and Super P conductive carbon black at a ratio of 84:10:6 by mass was suspended in N-methyl-2-pyrrolidene (NMP) and then homogenized to form a uniform slurry. The slurry was then cast on aluminum foil using the doctor blade technique to form a thin cathode film. The cathode film was dried in a vac-uum oven at 130 °C for 16 h. To improve adhesion, the cathode was calendered to form a thin film 23 μm thick. Small, round, cathode discs (diameter 14 mm) were punched out of the dry film for the 2032 coin-type test batteries. The batteries were assembled in an argon-filled glove box. Thin Li foil (0.5 mm thick, FMC lithium) was employed as the anode and a polypropylene membrane (Celgard 2400) was used as the separator. The electrolyte was 1 M $LiPF_6$ in ethylene carbonate/diethyl carbonate solution (EC:DEC = 1:2 by weight, Ferro). The electrochemical performance of $LiMn_2O_4$ pow-der was tested with a MACCOR (Model 4200) battery tester. The initial charge/discharge capacity was measured between 2.5 and 4.3 V, and the cycling performance between 3.0 and 4.3 V was measured at various C-rates (charge/discharge rates). All of the electrochemical performance measurements were obtained at a constant temperature of 30 °C.

3. Results and discussion

To understand the formation mechanism of the spinel $LiMn_2O_4$ in the pyrolysis flame, the thermal properties of the precur-sors $LiNO_3$ and $Mn(NO_3)_2 \cdot 4H_2O$ were studied by TGA analysis. Three experiments were performed: (1) $Mn(NO_3)_2 \cdot 4H_2O$ only, (2) $LiNO_3$ only, and (3) a stoichiometric amount of $LiNO_3$ and
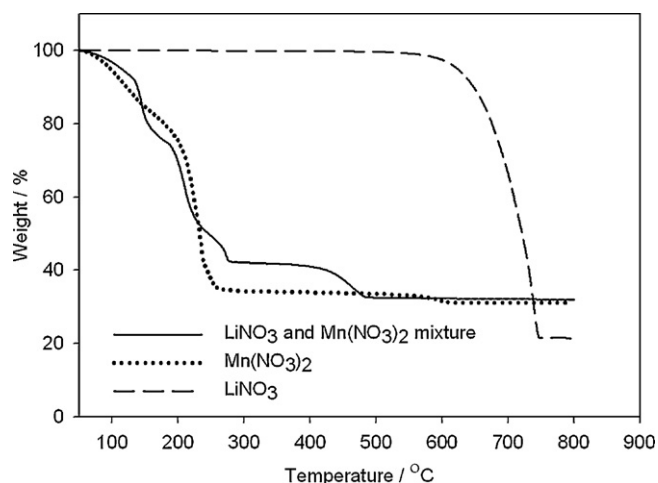
Fig. 2. TGA measurements of the individual precursor $LiNO_3$, and $Mn(NO_3)_2 \cdot 4H_2O$, and their mixture (Li:Mn = 1:2).

$Mn(NO_3)_2 \cdot 4H_2O$, all in methanol. The decomposition reaction mechanisms of $Mn(NO_3)_2$ and $LiNO_3$ are known, and their decomposition products are MnO_2 and Li_2O, respectively [33]. As indicated by the dotted-line in Fig. 2, pure $Mn(NO_3)_2$ decomposed into oxides in the temperature range of 200–280 °C, as indicated by the large weight loss. Pure $LiNO_3$ began to decompose at around 600 °C and was fully decomposed by 750 °C, as indicated by the dash-line. However, as shown by the solid-line, the complete decomposition of the mixture of precursors occurred at 480 °C, more than 200 °C less than that of the pure $LiNO_3$ salt. For a 1:2 molar ratio of $LiNO_3$ and $Mn(NO_3)_2 \cdot 4H_2O$ precursors, the total weight loss was calculated to be 57.5%, assuming complete decomposition of $Mn(NO_3)_2 \cdot 4H_2O$ to MnO_2, and the measured weight loss from TGA was 57.6% at 280 °C. Similarly, for complete decomposition of $LiNO_3$ to Li_2O, the calculated weight loss was 66.9%, compared to a measured weight loss of 67.1% at 480 °C. Thus, the assumed decomposition products were valid even for the mixture of nitrate precursors. Importantly, the decomposition temperature of $LiNO_3$ was much lowered in the mixture than alone. The lower decomposition temperature of $LiNO_3$ for mixtures has also been observed using a mixture of electrolytic manganese dioxide MnO_2 and $LiNO_3$ [34]. This was understood to be due to the presence of MnO_2, acting as a catalyst for the pyrolysis reactions [34].

The visible flame used to produce spinel $LiMn_2O_4$ was about 15 cm tall. Both H_2 and methanol are combustible and their oxidation provides heat for the synthesis reaction of spinel $LiMn_2O_4$. Temperature was measured along the axis with a Pt/Rh thermocouple (bead size = 340 μm). Fig. 3 shows axial temperature profile, uncorrected for radiation heat loss, as a function of the height above the burner (HAB). The highest temperature in the flame was 1100 °C and occurred at 13.4 cm HAB. This temperature was higher than the temperatures associated with the solid-state reaction, spray pyrolysis, and sol–gel methods, which are in the range of 200–1000 °C [6,35,36]. Nonetheless, the residence time of the aerosol at this temperature (1100 °C) was only milliseconds. The flame temperature could not be lowered further in the current setup without causing the flame to become unstable.

The formation of spinel $LiMn_2O_4$ in the flame is expected to follow a sequence of (1) evaporation of the methanol solvent, (2) pyrolysis of the precursors, (3) synthesis reactions of spinel $LiMn_2O_4$, and (4) sintering and coarsening of the primary particles. In the center of the flame, the temperature increased slowly until 5.0 cm HAB and then the temperature increased rapidly, as seen in Fig. 3. At this point, the solvent methanol would begin to evaporate quickly, as the temperature (>220 °C) was far above

its boiling point (∼65 °C). After evaporation, the Li and Mn nitrate precursors would begin to precipitate. Based on the TGA data, the precursor $Mn(NO_3)_2$ should start to decompose almost immediately upon evaporation of the solvent in the flame. Up until 7 cm HAB, the temperature was less than 430 °C, where $LiNO_3$ would begin to decompose. The temperature increased rapidly beyond this point, which is expected to lead to rapid thermal decomposition of the $LiNO_3$ and $Mn(NO_3)_2$ precursors. Further downstream in the flame, the particles coarsen and sinter. In the post-flame region (15–30 cm HAB), the temperature dropped slowly, allowing the nano-grains to grow into larger crystallites.

A characteristic residence time of the precursors/product in the flame reactor can be estimated by assuming the particles follow the flow field and neglecting buoyancy in the flame (if buoyancy is considered, the residence time will be shorter). The length scale is considered to be 30 cm because beyond 30 cm HAB, the temperature was less than 400 °C, so sintering of $LiMn_2O_4$ would be negligible. At a total flow rate of 3.0 L min^{-1} ($H_2 + N_2$), the characteristic residence time was calculated to be less than 800 ms, which is the shortest synthesis time among current synthesis methods for spinel $LiMn_2O_4$. For ultrasonic spray pyrolysis, sol–gel and solid-state reaction methods, it takes seconds to hours to synthesize nanocrystalline $LiMn_2O_4$ powders [2,6,11]. The short formation times were due to the rapid evaporation of solvent methanol, followed by rapid decomposition reactions of precursors and synthesis reactions of the spinel in the flame. At the high flame temperature, the solvent methanol also reacted as a fuel supporting local heat release in the flame. Thus, the FAST process is a rapid process to make $LiMn_2O_4$ powder continuously with low energy requirements.

The XRD pattern of the as-synthesized powder matched the spinel $LiMn_2O_4$ structure, as indicated by the strong intensities of the (1 1 1), (3 1 1) and (4 0 0) planes, as seen in Fig. 4(a). The wide XRD peaks of the as-synthesized powder indicated a nanocrystalline structure. The elemental ratio of Li and Mn was 1.01:2 as measured by ICP-MS analysis, which is consistent with spinel $LiMn_2O_4$. However, some impurities coexisted with the as-synthesized powder, as indicated by the minor peaks in the XRD spectrum. The impurity was identified as Mn_3O_4, which is known to form at elevated temperatures. Studies have shown that at elevated temperatures, oxygen may be extracted from spinel $LiMn_2O_4$, forming oxygen deficient spinel [37–39]. If the temperature exceeds 1000 °C, the spinel would eventually decompose into orthorhombic $LiMnO_2$ and Mn_3O_4, and release O_2 in an oxy-
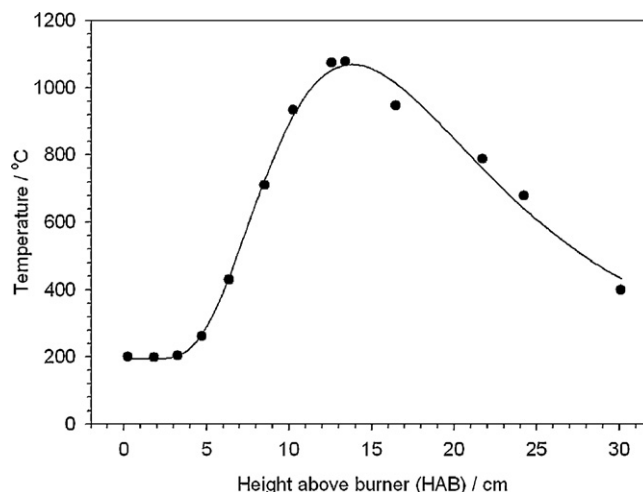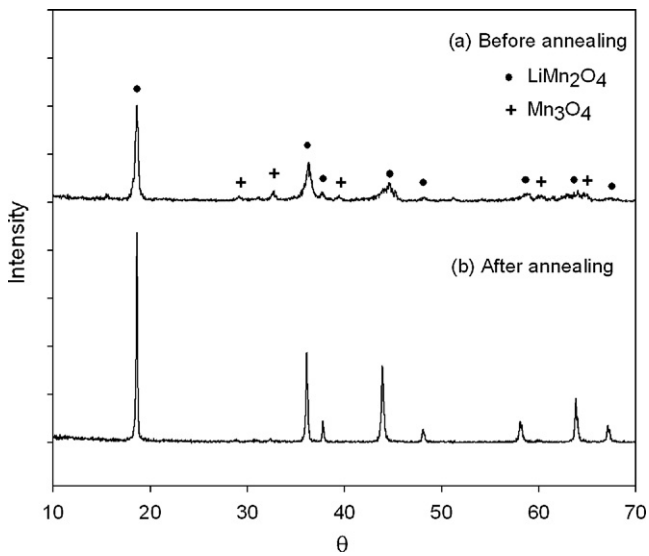

Fig. 3. Measured centerline temperature as a function of height above burner (HAB). Temperatures are not corrected for radiative heat loss from the thermocouple.

Fig. 4. XRD patterns of the flame-synthesized $LiMn_2O_4$ powder: (a) before annealing and (b) after annealing at 700 °C for 2 h.

gen extraction reaction [38]. In the flame, the residence time of the particles in the high temperature region was very short, so only a small portion of spinel $LiMn_2O_4$ decomposed into Mn_3O_4 in the flame. Nonetheless, a post-annealing treatment was necessary to remove the impurity in the flame-synthesized spinel $LiMn_2O_4$.

After annealing the as-synthesized powder at 700 °C for 2 h, the XRD pattern was a good match to the single-phase spinel $LiMn_2O_4$ with a space group $Fd\bar{3}m$, as shown in Fig. 4(b). No Mn_3O_4 impurity was detectable in the XRD spectrum. The crystallinity of the powder was also greatly improved, as indicated by the sharper XRD peaks. After Rietveld cell refinement, the lattice parameter a of the annealed powder was 8.234 Å, which is in good agreement with spinel $LiMn_2O_4$. The average grain size of the annealed powder

was 33 nm, as estimated by the Scherrer formula ($fwhm = 0.268°$, $2\theta = 43.981°$, $\lambda_{Cu/K-\alpha 1} = 1.54$ Å).

The SEM and TEM photographs of $LiMn_2O_4$ powder, before and after annealing are shown in Fig. 5. The as-synthesized particles were submicron in size, with some particles falling into the nano-size range, as seen from Fig. 5(a). The secondary particles consisted of irregular-shape, nano-size primary particles. The porous morphology of the as-synthesized powder was similar to that of the powder made with spray pyrolysis when using $LiNO_3$ and $Mn(NO_3)_2$ as precursors [11,15], however, the particle surface appeared smoother after annealing. The as-synthesized $LiMn_2O_4$ powder also showed a polycrystalline structure, as seen in the TEM image of Fig. 5(b). The size distribution of the as-synthesized aerosol is shown in Fig. 6(a) as measured by SMPS. The geometric mean diameter of the as-synthesized powder was 160 nm with a geometric standard derivation σ_g of 1.58. After annealing, the nano-sized particles did not exist, as can be seen by comparing the images of Fig. 5(a) with (c), and (b) with (d), and the powder showed a clearer facet structure, as compared to the as-synthesized powder. By measuring 390 different particles in the SEM images, the size distribution of the annealed powder was obtained, as shown in Fig. 6(b). The geometric mean diameter of the annealed powder was 330 nm with a geometric standard derivation, σ_g, of 1.81.

2032 coin-type half-cells were assembled with the unannealed (as-synthesized) and annealed $LiMn_2O_4$ powder as active cathode materials, and the cells were charged/discharged between 2.5 and 4.3 V at 0.1 C rate (1 C = 120 mAh g^{-1}). As seen in Fig. 7(a), the initial charge/discharge curve shows the characteristic voltage plateaus at 2.8 V and 4 V vs. Li, corresponding to spinel $LiMn_2O_4$ with an $Fd\bar{3}m$ space group structure. The initial charge and discharge capacity of the unannealed powder was about 70 mAh g^{-1} at 4 V, which is much lower than the theoretical capacity of $LiMn_2O_4$ (148 mAh g^{-1}). Nonetheless, the result was quite consistent with the measured capacity of nanocrystalline spinel $LiMn_2O_4$, which is from 70 to 100 mAh g^{-1} in the 4 V range [13]. The lower capacity at 4 V than the theoretical value for the as-synthesized powder can be explained by the large surface area, lower crystallinity [13,40,41], and also by the level of impurities in the powder. In the 3.0 V
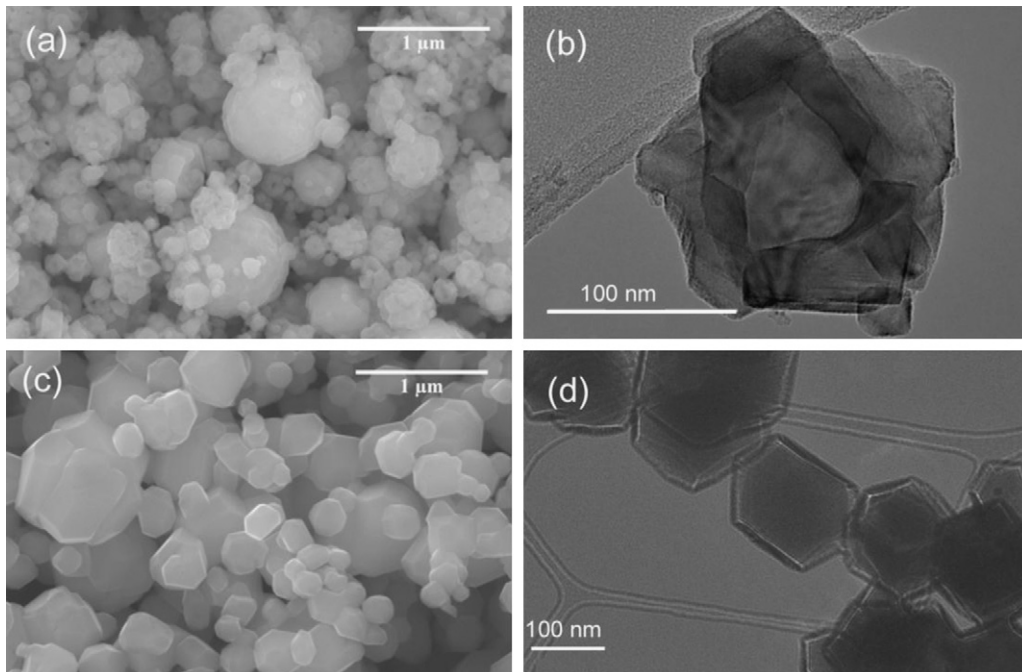
Fig. 5. Morphology of the $LiMn_2O_4$: (a) SEM of the powder before annealing; (b) TEM of the powder before annealing; (c) SEM of the powder after annealing; (d) TEM of the powder after annealing at 700 °C for 2 h (SEM: scale bar = 1 μm; TEM: scale bar = 100 nm).
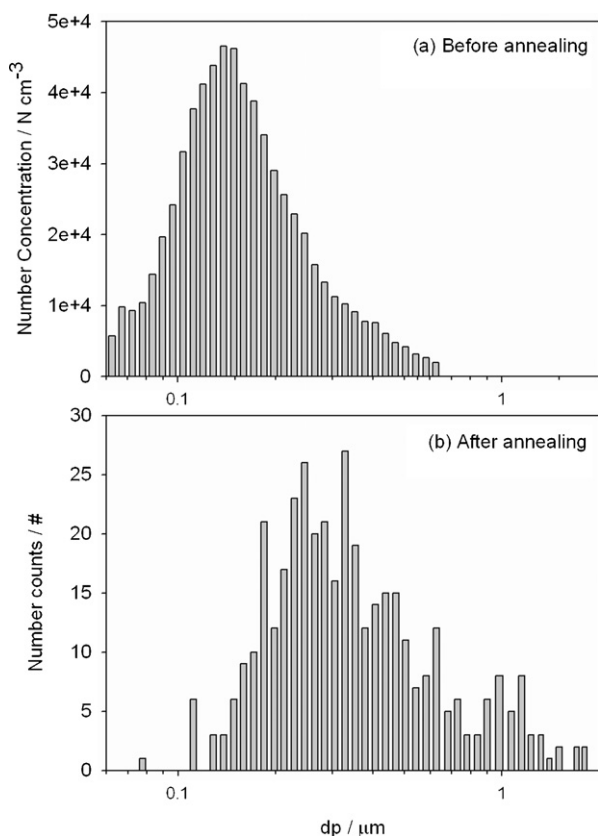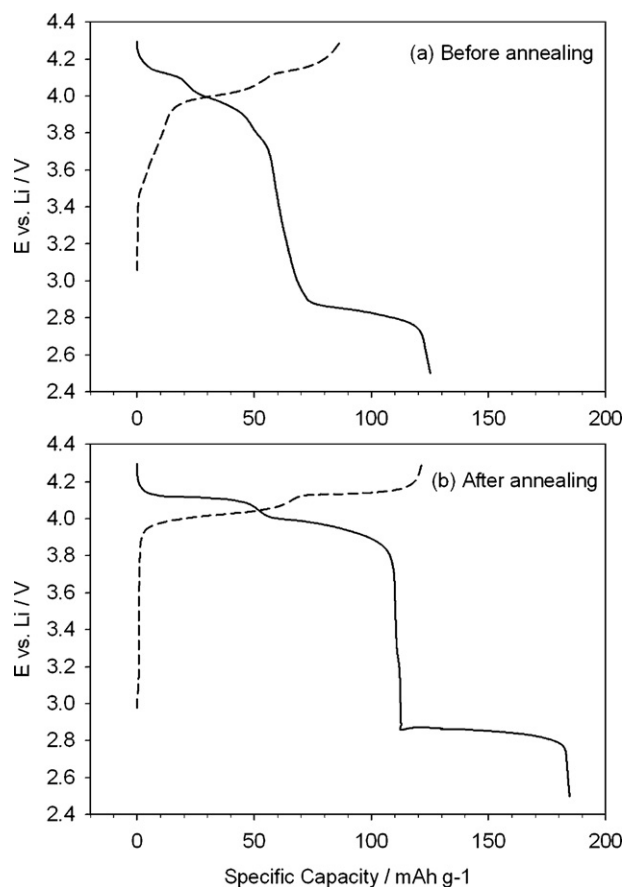
Fig. 6. Size distribution of the flame-synthesized LiMn$_2$O$_4$ powder: (a) before annealing and (b) after annealing at 700 °C for 2 h.

Fig. 7. Initial charge/discharge curve of the flame-synthesized LiMn$_2$O$_4$ powder: (a) before annealing and (b) after annealing at 700 °C for 2 h (dash line: charge curve; solid line: discharge curve).

range, the initial discharge capacity of unannealed powder was about 60 mAh g^{-1}, which is also lower than the theoretical value of LiMn$_2$O$_4$. This could be due to the oxygen deficiency of the spinel LiMn$_2$O$_4$ which can lead to a large capacity loss in the 3 V range. As discussed earlier, Mn$_3$O$_4$ was detected in the as-synthesized powder. Mn$_3$O$_4$ was not electrochemically active, so its presence lowered the capacities in both the 3 V and 4 V range. Due to the low overall capacity, the cell made with unannealed LiMn$_2$O$_4$ powder was not subject to further testing.

As shown in Fig. 7(b), after annealing, the LiMn$_2$O$_4$ powder showed a clearer two-staged lithium intercalation behavior at a voltage of 3.9 V and 4.16 V, which is indicative of a single-phase spinel LiMn$_2$O$_4$ structure. The initial charge and discharge capacities were about 120 mAh g^{-1} and 115 mAh g^{-1}, respectively, in the 4 V range. The reversible discharge capacity was 96% in the first cycle. The initial charge/discharge capacity was dramatically improved when compared to the as-synthesized powder because of the improved crystallinity and lack of impurities. However, the trend of the initial discharge curve in the entire range from 2.5 to 4.3 V was similar to that of slightly oxygen-deficient spinel LiMn$_2$O$_4$, for which the capacity in the 3 V range was low, about 70 mAh g^{-1} [37]. Although the oxygen extraction reaction, which leads to oxygen deficiency, is a reversible process, the oxygen vacancy in the spinel may not have been completely recovered by annealing at 700 °C for 2 h.

The rate capability of the annealed LiMn$_2$O$_4$ powder was evaluated at various C-rates, from 0.1 C to 2.0 C (1 C = 120 mAh g^{-1}) with a cut-off voltage of 3.0–4.3 V. The charge/discharge rate was increased every five cycles, as indicated in Fig. 8. In the first 10 cycles, the capacity of the cell rapidly faded from 115 mAh g^{-1} to 104 mAh g^{-1} at a charge/discharge rate from 0.1 C to 0.2 C. At the 11th cycle, a transitional cycle from 0.2 C to 0.5 C rates, the

capacity dropped dramatically, and then the cell showed a better capacity retention with an average coulombic efficiency of 99% at 0.5 C rate. At the transition from 1 C to 2 C, the cell also showed a large capacity loss with a coulombic efficiency of about 92%. In the next few cycles at 2 C, the cell showed less capacity loss with an average coulombic efficiency of 98%. The capacity fading was also observed in the annealed flame-synthesized spinel LiMn$_2$O$_4$. The reasons for capacity fading are understood to be manganese dissolution, electrolyte decomposition at high potentials, and the loss of
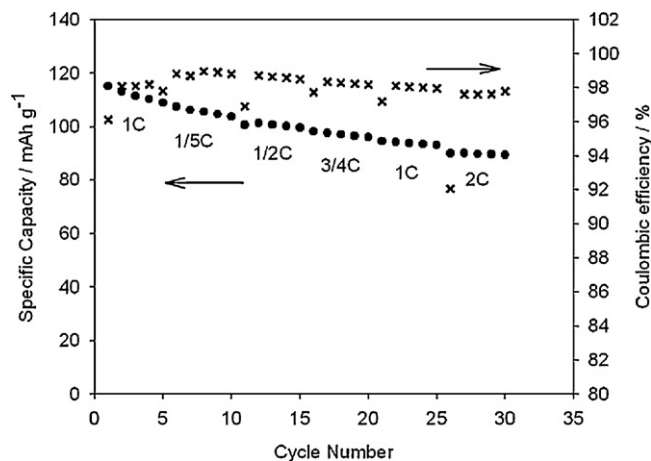
Fig. 8. Cycle performance of annealed powder with a cut-off voltage of 3.0–4.3 V at an increasing charge/discharge rate. Coulombic efficiency is calculated for each cycle.

crystallinity during cycling [42]. In addition, the small amount of oxygen deficiency may have been another reason for the capacity fading of the annealed $LiMn_2O_4$ [39]. Nonetheless, considering that only 6 wt% conductive carbon black was added to the cathode, the annealed flame-synthesized powder showed an acceptable cycling performance at increasing C-rates.

4. Conclusion

Nanostructured spinel $LiMn_2O_4$ cathode materials for lithium-ion batteries were synthesized by using flame-assisted spray technology (FAST). The as-synthesized powder showed a nano-crystalline structure with uniform morphology. However, the impurity Mn_3O_4 was detected, which resulted from the decomposition reaction of $LiMn_2O_4$ at elevated temperature ($>1000\,°C$). After a post-annealing treatment, the $LiMn_2O_4$ powder showed a single-phase spinel structure. The charge/discharge performance of the powder before and after post-annealing was in good agreement with the electrochemical characteristics of spinel $LiMn_2O_4$. However, the annealed $LiMn_2O_4$ powder had a much higher capacity than the as-synthesized powder, especially in the 4 V range. Moreover, the annealed $LiMn_2O_4$ powder showed a good rate capability with a small amount of conductive material. This paper has demonstrated that the FAST process has the potential to rapidly produce electrochemically active materials for lithium-ion secondary batteries at low cost.

Acknowledgements

References

[1] J.M. Tarascon, W.R. McKinnon, F. Coowar, T.N. Bowmer, G. Amatucci, D. Guyomard, J. Electrochem. Soc. 141 (1994) 1421–1431.
[2] M.M. Thackeray, W.I.F. David, P.G. Bruce, J.B. Goodenough, Mater. Res. Bull. 18 (1983) 461–472.
[3] S.-H. Kang, J.B. Goodenough, L.K. Rabenberg, Chem. Mater. 13 (2001) 1758–1764.
[4] S.R. Sahaya Prabaharan, M. Siluvai Michael, T. Prem Kumar, A. Mani, K. Athinarayanaswamy, R. Gangadharan, J. Mater. Chem. 5 (1995) 1035–1037.
[5] W. Liu, C.C. Farrington, F. Chaput, B. Dunn, J. Electrochem. Soc. 143 (1996) 879–884.
[6] Y.-K. Sun, I.-H. Oh, K.Y. Kim, Ind. Eng. Chem. Res. 36 (1997) 4839–4846.
[7] S. Komaba, N. Kumagai, M. Baba, F. Miura, N. Fujita, H. Groult, D. Devilliers, B. Kaplan, J. Appl. Electrochem. 30 (2000) 1179–1182.
[8] N. Treuil, C. Labrugere, M. Menetrier, J. Portier, G. Campet, A. Deshayes, J.-C. Frison, S.-J. Hwang, S.-W. Song, J.-H. Choy, J. Phys. Chem. B 103 (1999) 2100–2106.
[9] A.A. Van Zomeren, E.M. Kelder, J.C.M. Marijnissen, J. Schoonman, J. Aerosol Sci. 25 (1994) 1229–1235.
[10] T. Ogihara, N. Ogata, K. Katayama, Y. Azuma, N. Mizutani, Electrochemistry 68 (2000) 162–166.
[11] I. Taniguchi, C.K. Lim, D. Song, M. Wakihara, Solid State Ionics 146 (2002) 239–247.
[12] C. Wan, Y. Nuli, Q. Wu, M. Yan, Z. Jiang, J. Appl. Electrochem. 33 (2003) 107–112.
[13] S.-H. Park, S.-T. Myung, S.-W. Oh, C.S. Yoon, Y.-K. Sun, Electrochim. Acta 51 (2006) 4089–4095.
[14] J.P. Tu, H.M. Wu, Y.Z. Yang, W.K. Zhang, Mater. Lett. 61 (2007) 864–867.
[15] H. Ogihara, H. Aikiyo, N. Ogata, K. Katayama, Y. Azuma, J. Soc. Powder Technol. 38 (2001) 396–400.
[16] I. Taniguchi, N. Fukuda, M. Konarova, Powder Technol. 181 (2008) 228–236.
[17] M. Kojima, I. Mukoyama, K. Myoujin, T. Kodera, T. Ogihara, Key Eng. Mater. 388 (2009) 85–88.
[18] K. Myojin, T. Ogihara, N. Ogata, N. Aoyagi, H. Aikiyo, T. Ookawa, S. Omura, M. Yanagimoto, M. Uede, T. Oohara, Adv. Powder Technol. 15 (2004) 397–403.
[19] C.J. Unrau, R.L. Axelbaum, P. Biswas, P. Fraundorf, Proc. Combust. Inst. 31 (2007) 1865–1872.
[20] R.L. Vander Wal, T.M. Ticich, J. Phys. Chem. B 105 (2001) 10249–10256.
[21] H.K. Kammler, L. Mädler, S.E. Pratsinis, Chem. Eng. Technol. 24 (2001) 583–596.
[22] W.J. Stark, S.E. Pratsinis, Powder Technol. 126 (2002) 103–108.
[23] G.P. Fotou, S.J. Scott, S.E. Pratsinis, Combust. Flame 101 (1995) 529–538.
[24] X. Qin, Y. Ju, S. Bernhard, N. Yao, J. Mater. Res. 20 (2005) 2960–2968.
[25] D.P. Dufaux, R.L. Axelbaum, Combust. Flame 100 (1995) 350–358.
[26] R.L. Axelbaum, D.P. DuFaux, C.A. Frey, K.F. Kelton, S.A. Lawton, L.J. Rosen, S.M.L. Sastry, J. Mater. Res. 11 (1996) 948–954.
[27] J.L. Barr, R.L. Axelbaum, M.E. Macias, J. Nanopart. Res. 8 (2006) 11–22.
[28] R.L. Axelbaum, C.R. Lottes, J.I. Huertas, L.J. Rosen, Proc. Combust. Inst. 26 (1996) 1891–1897.
[29] H. Jang, C. Seong, Y. Suh, H. Kim, C. Lee, Aerosol Sci. Technol. 38 (2004) 1027–1032.
[30] F.O. Ernst, H.K. Kammler, A. Roessler, S.E. Pratsinis, W.J. Stark, J. Ufheil, P. Novak, Mater. Chem. Phys. 101 (2007) 372–378.
[31] T.J. Patey, R. Buchel, S.H. Ng, F. Krumeich, S.E. Pratsinis, P. Novak, J. Power Sources 189 (2009) 149–154.
[32] T.J. Patey, R. Büchel, M. Nakayama, P. Novák, Phys. Chem. Chem. Phys. 11 (2009) 3756–13756.
[33] K.H. Stern, High Temperature Properties and Thermal Decomposition of Inorganic Salts with Oxyanions, CRC Press, 2000.
[34] N. Kumagai, T. Saito, S. Komaba, J. Appl. Electrochem. 30 (2000) 159–163.
[35] D. Guyomard, J.M. Tarascon, J. Electrochem. Soc. 139 (1992) 937–948.
[36] S.H. Ju, D.Y. Kim, E.B. Jo, Y.C. Kang, J. Mater. Sci. 42 (2007) 5369–5374.
[37] A. Yamada, K. Miura, K. Hinokuma, M. Tanaka, J. Electrochem. Soc. 142 (1995) 2149–2156.
[38] J.M. Tarascon, F. Coowar, G. Amatuci, F.K. Shokoohi, D.G. Guyomard, J. Power Sources 54 (1995) 103–108.
[39] J.Y. Lee, Y. Hideshima, Y.-K. Sun, M. Yoshio, J. Electroceram. 9 (2002) 209–214.
[40] C.J. Curtis, J. Wang, D.L. Schulz, J. Electrochem. Soc. 151 (2004) 590–598.
[41] C.-Z. Lu, G.T.-K. Fey, J. Phys. Chem. Solids 67 (2006) 756–761.
[42] I. Taniguchi, D. Song, M. Wakihara, J. Power Sources 109 (2002) 333–339.